

# HOPE: An Automatically Differentiable High-Order Non-Oscillatory Finite-Volume Shallow-Water Dynamic Core

Zhou Lilong<sup>1,2</sup>

1. *Tsinghua University, Beijing, China*

2. *CMA Earth System Modeling and Prediction Centre (CEMC), Beijing, China*

**Corresponding author:** Zhou Lilong (zhoull@cma.gov.cn)

**Key words:** Automatic differentiation; High-order accuracy; Non-Oscillation; Finite-volume methods; Shallow-water Equations; Dynamic core.

## Abstract

An automatically differentiable, high-order non-oscillatory finite volume shallow water dynamic core has been constructed on a cubed sphere grid. This dynamic core has four advantageous properties: high order accuracy, essential non-oscillation, mass conservation, and scalability. Besides, the code development is based on PyTorch, enabling the model to run seamlessly on both CPU and GPU, while naturally possessing the capability of automatic differentiation. We named the new dynamic core as High Order Prediction Environment (HOPE). The spatial reconstruction is based on the two-dimensional tensor product polynomial and the genuine two-dimensional Weighted Essentially Non-Oscillatory (WENO) scheme. A novel panel boundary approach ensures that the accuracy can reach arbitrary order. These algorithms have very high degree of compatibility with GPU architecture, allowing the computational overhead to be mitigated through the utilization of GPU. The LMARS (Low Mach number Approximate Riemann Solver) scheme is adopted as Riemann solvers to determine fluxes on the Gaussian points on edges. Flux across the interface between each cell edge is computed using Gaussian quadrature, and the tendencies of prognostic variables are obtained by integration all the fluxes across the cell boundaries. This shallow water dynamic core demonstrates outstanding performance in ideal shallow water test cases. In the steady-state geostrophic flow, the 11th order scheme reduces errors to nearly round-off error even on coarse grids ( $2^\circ \times 2^\circ$ ). Furthermore, the Rossby-Haurwitz wave preserves its shape for over 90 days. To test the non-oscillation property, we designed a cylinder dam break case. The WENO approach effectively suppresses non-physical oscillation, and the genuine two-dimensional reconstruction exhibits significantly better isotropy than the dimension-by-dimension scheme.

## 1. Introduction

Numerical weather prediction (NWP) became a foundation of weather forecasting in past decades. The horizontal resolution of operational models in each NWP center is now finer than 10km, European Centre for Medium-Range Weather

Forecasts (ECMWF) enabled real-time global weather forecasting with about 9km horizontal grid since 2016[22], and Numerical Weather Prediction Center (NWPC) of China Meteorological Administration (CMA) increased the operational regional model resolution to 3km in 2017[9]. Finer resolution brings us not only more details about atmosphere, but also more challenge about simulating small synoptic systems, steeper topography and especially more computational cost.

In recent years, the machine learning (ML) technology has been widely utilized in atmospheric numerical simulations. Some research suggests that ML can overcome the challenge of computational cost and even improve the forecast accuracy. There are several common methods of leveraging ML in weather prediction. A simple and effective method is to apply machine learning to post-processing of model data, using neural networks to correct the model forecast fields so that the forecast results are closer to actual observations[39]. However, this type of method has limited effectiveness in correcting forecast results. Since it uses model forecasts as the source data, when the model forecasts have significant deviations, the correction effectiveness also diminishes.

Another method is establishing a data driven NN model to surrogate the entire prediction process, such as Pangu-Weather[2], FengWu[5], GraphCast[15], NowcastNet [41] and so on. The NN models perform excellent forecasting accuracy for the large-scale atmosphere state, meanwhile they are thousand times faster than traditional numerical mode. However, training these models require amount of reanalysis data, and the training process is very expensive, it costs hundreds of GPU to execute the training over weeks, and the forecasting becomes blurrier along with the leading time increase.

Some researchers attempted to merge the traditional NWP model and NN into a hybrid model. In the traditional NWP model, the solving process of governing equation is separated to dynamic part and physical part. The purpose of dynamic part is solving the grid-scale dynamic partial differential equation (PDE) by numerical methods, i.e. finite volume (FV), finite difference (FD), discontinuous Galerkin (DG) and so on. The physical part deals with the sub-grid physical processes by parameterization, which causes significant larger uncertainties and errors than dynamic part [28]. However, machine learning algorithms happen to be well-suited for addressing such problem. Wang et al. (2022) [36] emulating physical parameterization through a surrogate model, then coupling with the numerical dynamic core. The surrogate model is trained offline, requiring the long-term execution of the original numerical model to extract input and output data from the physical parameterization module for use as labels. The offline training of physical parameterization module needs much less data than the full model surrogation scheme. However, during the time marching, the prediction error emerges as a nonlinear superposition of the dynamic error, which arises from solving PDE, and the physical error, stemming from the distortion introduced by parameterizing the physical process. Offline training is a purely data-driven approach, where the surrogate model lacks awareness of the underlying dynamic core's behavior.

A more thorough solution would be to develop the entire numerical model on a machine learning programming platform, such as TensorFlow or PyTorch[14]. In this scenario, the dynamic core is based on a traditional numerical PDE solver, while the physical parameterization module is a neural network (NN) trained using the backpropagation of prediction residuals. Unlike the second method, this approach couples the dynamic core error and the physical parameterization error through

backpropagation. Therefore, during the training process, the NN-based physical parameterization module can obtain more comprehensive residual information. NeuralGCM [14] proposed a hybrid model by combining a spectral numerical dynamic core and NN based physical parameterization model. The dynamic core based on governing equations imposes rigorous physical constraints on the model, which eliminates the blurriness present in purely data-driven models within the NeuralGCM framework. Additionally, the power spectra performance of NeuralGCM is superior to that of purely data-driven meteorological models.

For NeuralGCM, although the spectral dynamic core can provide theoretical infinite accuracy, the inherent shortcomings of the spectral model still persist. Specifically, it fails to preserve mass conservation, and the global nature of spectral expansion also restricts the scalability of this method.

To overcome above problems, we introduce a shallow water dynamic core named High Order Prediction Environment (HOPE). The contributions of this study are

- 1) We develop HOPE, a shallow water model has four advantageous properties: arbitrary high order accuracy, essential non-oscillation, mass conservation, and scalability.
- 2) We desire a novel high order ghost cell interpolation scheme for cubed sphere grid, it needs only one sparse matrix multiplication to reach arbitrary odd convergence order.
- 3) We implement genuine two-dimensional WENO on cubed sphere, comparing to the dimension-by-dimension scheme, the genuine two-dimensional provides less dimension split error.
- 4) HOPE is developed on PyTorch, the auto-differentiate capability is naturally obtained, it's easy to couple with any neural-network (NN) based functions, such as sub-grid physical parameterization.
- 5) The algorithms of the HOPE model primarily involve convolution and matrix multiplications, which are widely used in the artificial neural networks and highly compatible with GPUs. HOPE demonstrates excellent computational efficiency on GPU platforms.

High order accuracy is a very attractive property for designing a dynamic core, especially in high resolution atmosphere simulation. A model with high order accuracy dynamic core brings much less simulation error than the low order one in smooth region, on the other hand, a high order model is able to resolve more details than low order model, even if the resolution is equivalent or coarser. Plenty of researches have been made about implementing high order schemes in spherical shallow water model, Chen and Xiao[1] provided a multi-moment finite volume (MCV) scheme, with 3<sup>rd</sup> and 4<sup>th</sup> order accuracy, to establish the shallow water model on cubed sphere. Ii and Xiao[10] extended MCV based shallow water model to icosahedral grid with 3<sup>rd</sup> and 4<sup>th</sup> order accuracy. Katta et al.[12][13] compared 1D and 2D reconstruction on cubed sphere, the 1D scheme reduced the order to 2<sup>nd</sup> order even if using the 5<sup>th</sup> order dimension-by-dimension Weighted Essentially Non-Oscillatory (WENO) reconstruction, the fully 2D scheme was able to maintain high order accuracy in smooth shallow water test cases, but also higher computational cost than 1D scheme. This conclusion is also confirmed in our test, dimension-by-dimension scheme is not a reliable choice to establish a high order dynamic core on cubed sphere, furthermore, the loss of cross-derivative

terms leads to unreasonable anisotropy in the cylinder dam break case we describe in section 5.

Ullrich et al.[34][35] developed a high-order finite volume model, MOCRE, on cubed sphere, which took horizontal reconstruction by piecewise-parabolic and piecewise-cubic schemes. MOCRE has  $O(\Delta x^{k-1})$  order accuracy when the stencil width is  $k$ . In this paper, we expand tensor product polynomial in a square stencil with width  $k$ , and the model is  $O(\Delta x^k)$  accuracy. Ullrich et al. mentioned the accuracy can be arbitrary, but unfortunately, in our numerical test, the accuracy cannot higher than 7<sup>th</sup> once the ghost interpolation is one side scheme, oscillation occurs from corner zone of the panel when the stencil is  $9 \times 9$  or larger. We modified the ghost interpolation scheme to a central scheme, oscillation is eliminated and the accuracy can be arbitrary, we test the accuracy until 11<sup>th</sup> order to prove this property.

WENO is an adaptive numerical scheme, which is widely used in computational fluid dynamics (CFD) simulation, it is able to eliminate the non-physical oscillation caused by sharp discontinuous without reducing the accuracy in smooth region[11][19]. In previous researches about implementing WENO in atmospheric simulation, WENO has showed some attractive advantages. In the test case of density current[30], high order WENO schemes yield convergence solution in coarse resolution, while the centered schemes could not[29]. Lunet et al.[20] combined WENO and Explicit Runge-Kutta methods in Meso-NH model, WENO maintained better stable and non-oscillatory transitions with sharp discontinuities than centered scheme, and also improved computational efficiency. In the test case of colliding thermals, which was designed by Norman[23], non-physical oscillation was appeared without using WENO limiter, and a more conformal result was made by WENO scheme, even though the perturbation gradient was steep.

One of the challenges in developing a global atmospheric model is finding a method of discretizing the governing equations in spherical geometry[10]. The original WENO was constructed in one-dimensional case[19], and it was able to be extended to 2D by genuine 2D or dimension-by-dimension schemes. Shi et al.[31] mentioned genuine 2D scheme gave less error but cost more computational time. In another aspect, genuine 2D is easier to apply to complex geometric discretization, WENO 2D was developed in early study[31]. Recently, Zhu and Shu designed two-dimensional central WENO schemes on both regular and triangular mesh, the polynomial coefficients were computed by solving an overdetermined linear system in a least square sense[43][44][45]. Zhao et al. developed WENO on unstructured quadrilateral and triangular meshes[42].

We attempt to construct a dynamic core based on following considerations: Firstly, the basic the mass conservation is a basic property for a dynamic core[33][40], a finite volume scheme conserves local and global mass naturally. Secondly, the algorithm should be robust enough to deal with the fast wave and steep gradient, and also treat the slow wave with high accuracy[34], this requirement can be separated in two parts, the algorithm should be able to maintain high order accuracy in smooth region, and adapt to the large gradient in non-smooth region, non-physical oscillation should be eliminated by the numerical scheme, a WENO based limiter is preferred. Thirdly, since the computational cost increases fast with higher resolution, the dynamic core should be acceptable on massively parallel computation, hence combination of local finite volume reconstruction and Riemann solver is adopted in our algorithm.

In this paper, we provide a genuine 2D upwind WENO scheme on cubed sphere, which is able to maintain high order

convergence ratio in smooth cases, and limit the non-physical oscillation in the large gradient area. The crucial issues are determining the optimal linear weight in 2D space and ghost cell interpolation on cubed sphere.

Since the coordinates between two cube panels are discontinuous, careful ghost cell interpolation is necessary for reaching high order accuracy, we introduce panel boundary treatment in section 3.3.

## 2. Governing Equation on Cubed Sphere

Cubed sphere grid decomposes sphere to six panels, the computational space is structured and rectangular in each panel, these features make it easy to take high order reconstruction and massive threads parallel, details in Figure 2.1. The early research about solving primitive equation on cubed sphere can be found in Sadourny (1972)[30]. In recent decades, cubed sphere is used in different kinds of high order accuracy atmospheric models, Chen and Xiao[1] built a shallow water model by multi-moment constraint finite volume method on cubed sphere, 3<sup>rd</sup>~4<sup>th</sup> order accuracy was achieved. Ullrich et al.[34][35] developed a high order dynamic core based on cubed sphere, Nair et al.[24][25][26][27] established discontinuous Galerkin model on cubed sphere. In our research, cubed sphere is also adopted, even though the mesh is not orthogonal, we can still treat the computational space as rectangular grid by taking generalized curvilinear coordinate equation set. In this section, we introduce the shallow water equation set in generalized curvilinear coordinate, and special treatment of topography.

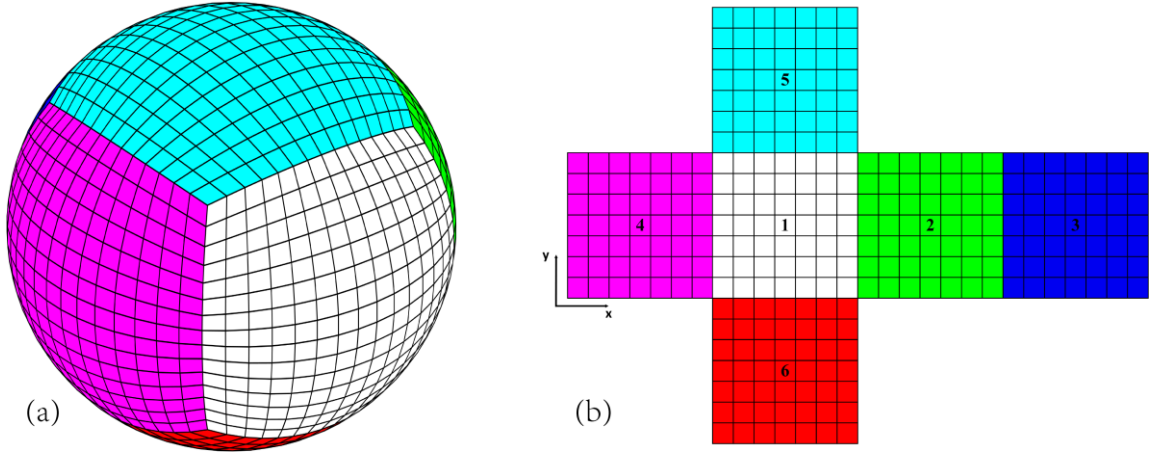


Figure 2.1 Cubed sphere grid. (a) Physical space; (b) Computational space. Six panels are identified by indices from 1 to 6.

Shallow water equation set on gnomonic equiangular cubed sphere grid is written as

$$\begin{cases} \frac{\partial \sqrt{G} \phi}{\partial t} + \frac{\partial \sqrt{G} \phi u}{\partial x} + \frac{\partial \sqrt{G} \phi v}{\partial y} = 0 \\ \frac{\partial \sqrt{G} \phi u}{\partial t} + \frac{\partial \sqrt{G} \left( \phi u u + \frac{1}{2} G^{11} \phi^2 \right)}{\partial x} + \frac{\partial \sqrt{G} \left( \phi u v + \frac{1}{2} G^{12} \phi^2 \right)}{\partial y} = \psi_M^1 + \psi_C^1 + \psi_B^1 \\ \frac{\partial \sqrt{G} \phi v}{\partial t} + \frac{\partial \sqrt{G} \left( \phi u v + \frac{1}{2} G^{21} \phi^2 \right)}{\partial x} + \frac{\partial \sqrt{G} \left( \phi v v + \frac{1}{2} G^{22} \phi^2 \right)}{\partial y} = \psi_M^2 + \psi_C^2 + \psi_B^2 \end{cases} \quad (2.1)$$

The gnomonic equiangular coordinates are represented by  $(x, y, n_p)$ , where  $(x, y) \in \left[-\frac{\pi}{4}, \frac{\pi}{4}\right]$  are local equiangular coordinate of each panel and  $n_p$  is panel number.  $\phi = gh$  is geopotential height,  $h$  is fluid thickness,  $u, v$  is contravariant wind in  $x, y$  direction,  $g$  is gravity acceleration.  $\psi_M, \psi_C, \psi_B$  are the metric term, Coriolis term and bottom topography influence term

$$\psi_M = \begin{pmatrix} \psi_M^1 \\ \psi_M^2 \end{pmatrix} = \frac{2\sqrt{G}}{\delta^2} \begin{pmatrix} -XY^2\phi_{uu} + Y(1+Y^2)\phi_{uv} \\ X(1+X^2)\phi_{uv} - X^2Y\phi_{vv} \end{pmatrix} \quad (2.2)$$

$$\psi_c = -\sqrt{G}\sqrt{G}f\mathbf{k} \times \phi\mathbf{u} = \sqrt{G}f \begin{pmatrix} -G^{12} & G^{11} \\ -G^{22} & G^{12} \end{pmatrix} \begin{pmatrix} \sqrt{G}\phi_u \\ \sqrt{G}\phi_v \end{pmatrix} \quad (2.3)$$

$$\psi_B = -\sqrt{G}\phi G^{ij} \frac{\partial \phi_s}{\partial x^j} = -\sqrt{G}\phi \begin{pmatrix} G^{11} \frac{\partial \phi_s}{\partial x} + G^{12} \frac{\partial \phi_s}{\partial y} \\ G^{21} \frac{\partial \phi_s}{\partial x} + G^{22} \frac{\partial \phi_s}{\partial y} \end{pmatrix} \quad (2.4)$$

where  $X = \tan x, Y = \tan y, \delta = \sqrt{1+X^2+Y^2}$ , and  $f = 2\Omega \sin\theta$  is Coriolis parameter, and  $\phi_s = gh_s$  is surface geopotential height,  $h_s$  is surface height.

$$\sin\theta = \begin{cases} Y/\delta, & n_p \in \{1,2,3,4\} \\ 1/\delta, & n_p = 5 \\ -1/\delta, & n_p = 6 \end{cases} \quad (2.5)$$

The contravariant metric on cubed-sphere is

$$G^{ij} = \frac{\delta^2}{r^2(1+X^2)(1+Y^2)} \begin{pmatrix} 1+Y^2 & XY \\ XY & 1+X^2 \end{pmatrix} \quad (2.6)$$

The covariant metric

$$G_{ij} = \frac{r^2(1+X^2)(1+Y^2)}{\delta^4} \begin{pmatrix} 1+X^2 & -XY \\ -XY & 1+Y^2 \end{pmatrix} \quad (2.7)$$

and the metric determinant is given by

$$\sqrt{G} = \sqrt{\det(G_{ij})} = \frac{r^2(1+X^2)(1+Y^2)}{\delta^3} \quad (2.8)$$

$r$  is radius of earth.

The contravariant wind vector  $\mathbf{V} = (u, v)$  can be convert to wind vector on spherical LAT/LON coordinate  $\mathbf{V}_s = (u_s, v_s)$

by the following formula

$$\begin{pmatrix} u_s \\ v_s \end{pmatrix} = J \begin{pmatrix} u \\ v \end{pmatrix} \quad (2.9)$$

where  $J$  is a  $2 \times 2$  conversion matrix, the expressions are different in each panel

$$J = r \begin{pmatrix} \cos\theta \frac{\partial \lambda}{\partial x} & \cos\theta \frac{\partial \lambda}{\partial y} \\ \frac{\partial \theta}{\partial x} & \frac{\partial \theta}{\partial y} \end{pmatrix} = \begin{cases} r \begin{pmatrix} \cos\theta & 0 \\ -\sin\theta \cos\theta \tan\lambda_p & \cos\lambda_p \cos^2\theta + \frac{\sin^2\theta}{\cos\lambda_p} \end{pmatrix}, & \text{panel 1~4} \\ r \begin{pmatrix} \cos\lambda \sin\theta \Gamma_1 & \sin\lambda \sin\theta \Gamma_2 \\ -\sin\lambda \sin^2\theta \Gamma_1 & \cos\lambda \sin^2\theta \Gamma_2 \end{pmatrix}, & \text{panel 5} \\ r \begin{pmatrix} -\cos\lambda \sin\theta \Gamma_1 & \sin\lambda \sin\theta \Gamma_2 \\ \sin\lambda \sin^2\theta \Gamma_1 & \cos\lambda \sin^2\theta \Gamma_2 \end{pmatrix}, & \text{panel 6} \end{cases} \quad (2.10)$$

$$\lambda_p = \lambda - \frac{\pi}{2}(i_{panel} - 1), \quad \Gamma_1 = 1 + \frac{\sin^2\lambda}{\tan^2\theta}, \quad \Gamma_2 = 1 + \frac{\cos^2\lambda}{\tan^2\theta} \quad (2.11)$$

where  $\lambda, \theta$  are longitude and latitude, and  $i_{panel}$  is the panel index as shown in Figure 2.1(b). The relation between  $J$  and  $G_{ij}$

is

$$G_{ij} = J^T J \quad (2.12)$$

In our numerical experiments, topography causes non-physical oscillation while we using equation set Eq.(2.1) and reconstructing  $\sqrt{G}\phi$ , as mentioned by [6], so called ‘‘C-property’’ needs to be preserved. Inspired by [10], we reconstruct  $\sqrt{G}\phi_t$  instead of  $\sqrt{G}\phi$ , where  $\phi_t = \phi + \phi_s$  is total geopotential height, and the reconstruction method is introduced in the next section. The momentum equations need to be modified as follow

$$\begin{cases} \frac{\partial\sqrt{G}\phi}{\partial t} + \frac{\partial\sqrt{G}\phi u}{\partial x} + \frac{\partial\sqrt{G}\phi v}{\partial y} = 0 \\ \frac{\partial\sqrt{G}\phi u}{\partial t} + \frac{\partial\sqrt{G}\left(\phi uu + \frac{1}{2}G^{11}\phi_t^2\right)}{\partial x} + \frac{\partial\sqrt{G}\left(\phi uv + \frac{1}{2}G^{12}\phi_t^2\right)}{\partial y} = \psi_M^1 + \psi_C^1 + \psi_B^1 \\ \frac{\partial\sqrt{G}\phi v}{\partial t} + \frac{\partial\sqrt{G}\left(\phi uv + \frac{1}{2}G^{21}\phi_t^2\right)}{\partial x} + \frac{\partial\sqrt{G}\left(\phi vv + \frac{1}{2}G^{22}\phi_t^2\right)}{\partial y} = \psi_M^2 + \psi_C^2 + \psi_B^2 \end{cases} \quad (2.13)$$

and the bottom topography influence term is now expressed as

$$\psi_B = \sqrt{G}\phi_s G^{ij} \frac{\partial\phi_t}{\partial x^j} = \sqrt{G}\phi_s \begin{pmatrix} G^{11} \frac{\partial\phi_t}{\partial x} + G^{12} \frac{\partial\phi_t}{\partial y} \\ G^{21} \frac{\partial\phi_t}{\partial x} + G^{22} \frac{\partial\phi_t}{\partial y} \end{pmatrix} \quad (2.14)$$

The reconstruction variables are  $(\sqrt{G}\phi_t, \sqrt{G}\phi u, \sqrt{G}\phi v)$ .

We write the governing equation set to vector form

$$\frac{\partial\mathbf{q}}{\partial t} + \frac{\partial\mathbf{F}(\mathbf{q})}{\partial x} + \frac{\partial\mathbf{G}(\mathbf{q})}{\partial y} = \mathbf{S}(\mathbf{q}) \quad (2.15)$$

$$\mathbf{q} = \begin{bmatrix} \sqrt{G}\phi \\ \sqrt{G}\phi u \\ \sqrt{G}\phi v \end{bmatrix}, \mathbf{F} = \begin{bmatrix} \sqrt{G}\phi u \\ \sqrt{G}\left(\phi uu + \frac{1}{2}G^{11}\phi_t^2\right) \\ \sqrt{G}\left(\phi uv + \frac{1}{2}G^{21}\phi_t^2\right) \end{bmatrix}, \mathbf{G} = \begin{bmatrix} \sqrt{G}\phi v \\ \sqrt{G}\left(\phi uv + \frac{1}{2}G^{12}\phi_t^2\right) \\ \sqrt{G}\left(\phi vv + \frac{1}{2}G^{22}\phi_t^2\right) \end{bmatrix}, \mathbf{S} = \begin{bmatrix} 0 \\ \psi_M^1 + \psi_C^1 + \psi_B^1 \\ \psi_M^2 + \psi_C^2 + \psi_B^2 \end{bmatrix} \quad (2.16)$$

### 3. Spatial Discretization

Finite volume method evaluates the temporal tendency of cell average by net flux, the flux across cell edges is able to be obtained by gaussian quadrature, we calculate the field value on gaussian quadrature point by spatial reconstruction and determine the flux value by Riemann solver. In this section, we introduce three two types of reconstruction methods, two-dimensional reconstruction by tensor product polynomial (TPP), and two-dimensional WENO based on tensor product polynomial (WENO2D). Reconstruction provides two values on each gaussian quadrature point (GQP), we use AUSM(Advection Upstream Splitting Method) [17][18] and LMARS (Low Mach number Approximate Riemann Solver)[4] schemes as Riemann solvers to determine the flux value, after that the flux across the edges between adjacent cells is obtained by linear gaussian quadrature on each edge.

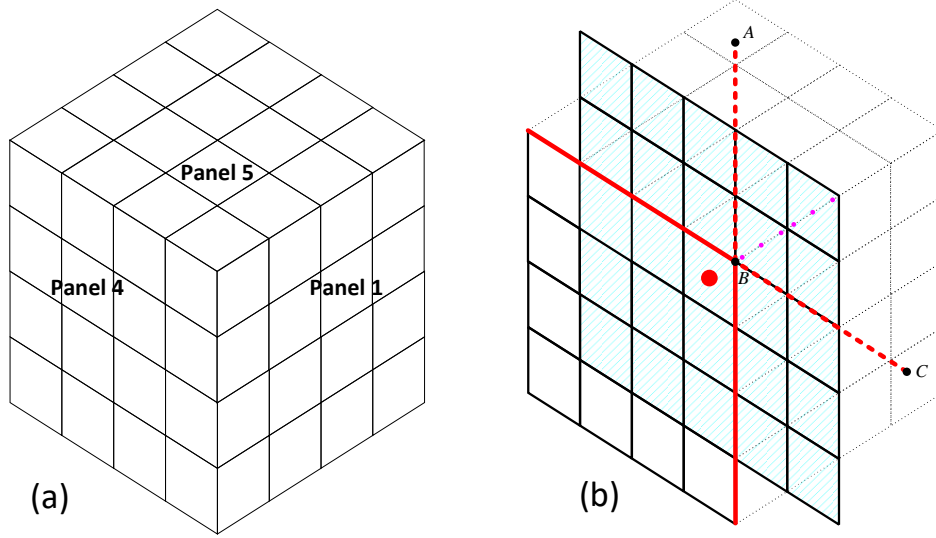


Figure 3.1 (a) Adjacent area of panels 1, 4 and 5. (b)  $5 \times 5$  reconstruction stencil nearby panel corner is represented by shade. The cell contains red dot is the target cell on panel 4, red solid lines are boundary of panel 4, red dash lines are extension line of panel 4 boundary line.  $A$  and  $C$  are points on dash line,  $B$  is the upper right corner point of panel 4.

According to the finite volume scheme, average Eq.(2.15) on cell  $i, j$ , we have

$$\frac{\partial \bar{q}_{i,j}}{\partial t} + \frac{\bar{F}_{i+\frac{1}{2},j} - \bar{F}_{i-\frac{1}{2},j}}{\Delta x} + \frac{\bar{G}_{i+\frac{1}{2},j} - \bar{G}_{i+\frac{1}{2},j}}{\Delta y} = \bar{S}_{i,j} \quad (3.1)$$

$$\frac{\partial \bar{q}_{i,j}}{\partial t} = \frac{1}{\Delta x \Delta y} \frac{\partial}{\partial t} \iint_{\Omega_{i,j}} \mathbf{q} \, dx \, dy, \quad \bar{S}_{i,j} = \frac{1}{\Delta x \Delta y} \iint_{\Omega_{i,j}} \mathbf{S} \, dx \, dy \quad (3.2)$$

$$\bar{F}_{i-\frac{1}{2},j} = \frac{1}{\Delta y} \int_{e_{i-\frac{1}{2}}} \mathbf{F} \, dy, \quad \bar{F}_{i+\frac{1}{2},j} = \frac{1}{\Delta y} \int_{e_{i+\frac{1}{2}}} \mathbf{F} \, dy \quad (3.3)$$

$$\bar{G}_{i,j-\frac{1}{2}} = \frac{1}{\Delta x} \int_{e_{j-\frac{1}{2}}} \mathbf{G} \, dx, \quad \bar{G}_{i,j+\frac{1}{2}} = \frac{1}{\Delta x} \int_{e_{j+\frac{1}{2}}} \mathbf{G} \, dx \quad (3.4)$$

where  $\Omega_{i,j}$  represents the region overlapped by cell  $(i, j)$ ,  $e_{i-\frac{1}{2}}, e_{i+\frac{1}{2}}, e_{j-\frac{1}{2}}, e_{j+\frac{1}{2}}$  are left, right, bottom, top edges of cell  $(i, j)$ .

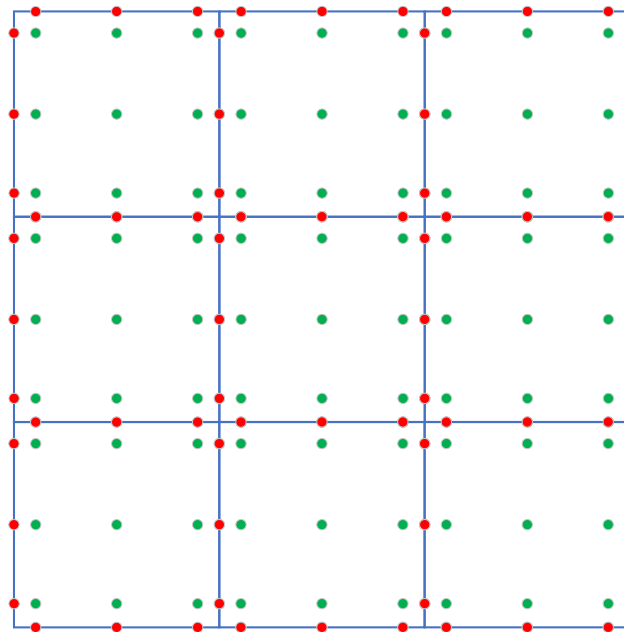


Figure 3.2 Function points on cell. Red points are edge quadrature points (EQP) or called flux points, green points are inner cell quadrature points (CQP).



The physical interpretation of equation Eq.(3.1) is that the average tendency of prognostic field  $\mathbf{q}$  within cell  $(i, j)$  is governed by the average net flux and average source. In this study, we calculate these averages using Gaussian quadrature, the function points within each cell are illustrated in Figure 3.2, the EQPs are share by adjacent cells, and CQPs are exclusive for each cell.

Average on edge by 1D scheme:

$$\bar{\mathbf{F}}_{i+\frac{1}{2}j} \approx \sum_{r=1}^{m_e} w_r \mathbf{F}_r = \mathbf{w} \mathbf{F}_r \quad (3.5)$$

where  $\mathbf{w} = (w_1, w_2, \dots, w_{m_e})$  is the 1D Gaussian quadrature coefficient matrix,  $m_e$  is the number of quadrature points on each edge.

Average in cell by 2D scheme:

$$\bar{\mathbf{S}}_{i,j} \approx \sum_{r=1}^{m_c} W_r \mathbf{S}_r = \mathbf{W} \mathbf{S}_r \quad (3.6)$$

where  $\mathbf{W} = (W_1, W_2, \dots, W_{m_c})$  is the 2D Gaussian quadrature coefficient matrix,  $m_c$  is the number of quadrature points on each cell.

### 3.1 Tensor Product Polynomial (TPP) Reconstruction

The computational space of cubed sphere is rectangular and structured, we adopt to take reconstruction on square stencil. A two-dimensional  $d$ -th degree polynomial has number of terms  $n = \frac{(d+1)(d+2)}{2}$ , it is not able to be fully filled by a  $k$ -th order square stencil ( $k \times k$  cells), as shown in Figure 3.3 (a).

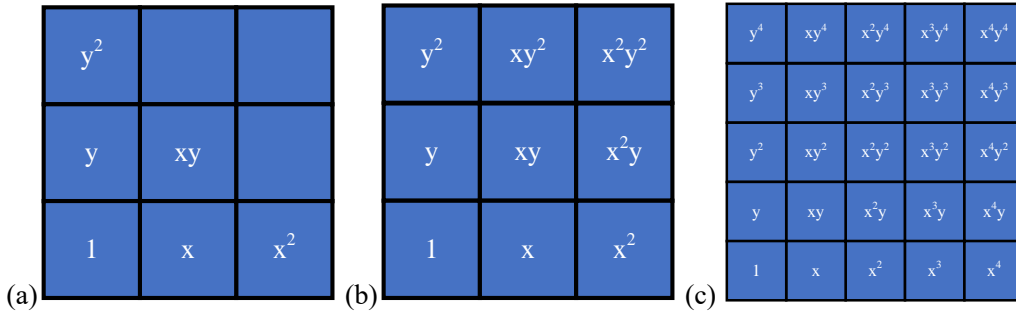


Figure 3.3 Polynomial terms on stencils. (a): 2<sup>nd</sup> degree polynomial stencil; (b): 3<sup>rd</sup> order TPP stencil; (c) 5<sup>th</sup> order TPP stencil

We make use of the TPP to approximate the horizontal reconstruction. A TPP is expressed as

$$p(x, y) = \sum_{i=1}^m \sum_{j=1}^n a_k x^{i-1} y^{j-1} = \sum_{k=1}^N a_k c_k(x, y) \quad (3.7)$$

where  $m$  and  $n$  are row and column of stencil.  $a_k$  is the coefficient of each term, the term index  $k = i + m(j - 1)$ , and  $c_k(x, y) = x^\alpha y^\beta$ ,  $\alpha = k - \text{int}\left(\frac{k-1}{n}\right)n$ ,  $\beta = \text{int}\left(\frac{k-1}{n}\right)$ ,  $\text{int}$  is the same function in Fortran,  $N$  is the cell number in stencil and also the term number of the TPP, the 3<sup>rd</sup> and 5<sup>th</sup> order stencils are shown in Figure 3.3. We define column vectors  $\mathbf{c}(x, y) = \{c_k(x, y) | k = 1, 2, 3, \dots, N\}$  and  $\mathbf{a} = \{a_k | k = 1, 2, 3, \dots, N\}$ , the point value on  $(x, y)$  can be written as

$$p(x, y) = \mathbf{c}(x, y) \cdot \mathbf{a} \quad (3.8)$$

The volume integration average (VIA) of evolution field  $q$  on cell  $\Omega_i$  is represented by

$$\bar{q}_i = \frac{1}{\Delta x_i \Delta y_i} \iint_{\Omega_i} p(x, y) dx dy \quad (3.9)$$

$\Delta x_i, \Delta y_i$  are length of edges  $x, y$  of cell  $\Omega_i$  in computational space. In our setting, all of the cells in the computational space are set to unit square, therefore  $\Delta x_i = 1, \Delta y_i = 1$ , and (3.9) becomes

$$\bar{q}_i = \iint_{\Omega_i} p(x, y) dx dy = \iint_{\Omega_i} \mathbf{c} \cdot \mathbf{a} dx dy = \boldsymbol{\psi}_i \cdot \mathbf{a} \quad (3.10)$$

where  $\boldsymbol{\psi}_i = \iint_{\Omega_i} \mathbf{c} dx dy = \begin{pmatrix} \iint_{\Omega_i} c_1 dx dy \\ \iint_{\Omega_i} c_2 dx dy \\ \vdots \\ \iint_{\Omega_i} c_N dx dy \end{pmatrix}$ , combining  $N$  cells, we have following linear system

$$A \mathbf{a} = \bar{\mathbf{q}} \quad (3.11)$$

where

$$A = \begin{pmatrix} \boldsymbol{\psi}_1^T \\ \boldsymbol{\psi}_2^T \\ \vdots \\ \boldsymbol{\psi}_N^T \end{pmatrix}, \bar{\mathbf{q}} = \begin{pmatrix} \bar{q}_1 \\ \bar{q}_2 \\ \vdots \\ \bar{q}_N \end{pmatrix} \quad (3.12)$$

and polynomial coefficient  $\mathbf{a}$  can be obtain by solving Eq.(3.11).

$$\mathbf{a} = A^{-1} \bar{\mathbf{q}} \quad (3.13)$$

The reconstruction values on  $M$  points can be obtained by following formula

$$P = C \mathbf{a} = C A^{-1} \bar{\mathbf{q}} = R \bar{\mathbf{q}} \quad (3.14)$$

where  $P = \begin{pmatrix} p(x_1, y_1) \\ p(x_2, y_2) \\ \vdots \\ p(x_M, y_M) \end{pmatrix}$ ,  $C = \begin{pmatrix} \mathbf{c}_1^T \\ \mathbf{c}_2^T \\ \vdots \\ \mathbf{c}_M^T \end{pmatrix}$ ,  $\mathbf{c}_j^T = \mathbf{c}^T(x_j, y_j), j = 1, 2, \dots, M$ , superscript  $T$  stands for transpose matrix, and

the reconstruction matrix

$$R = C A^{-1} \quad (3.15)$$

In our model,  $(x_j, y_j)$  represents the function points on target cell.

## 3.2 Genuine Two-Dimensional WENO

WENO is an adaptive algorithm, it takes high order accuracy in smooth area, and when the field is discontinuous, WENO reduce the accuracy to low order to capture the shock. Shi and Shu (2002)[31] mentioned a fifth-order finite volume WENO can be constructed in two different ways, ‘‘Genuine 2D’’ and ‘‘Dimension by Dimension’’, in genuine 2D case, a 3<sup>rd</sup> order stencil with  $3 \times 3$  cells can be decomposed by sub-stencils with  $2 \times 2$  cells, and a  $5 \times 5$  stencil can be decomposed to 9 sub-stencils, there are  $3 \times 3$  cells contained in each sub-stencil, details in Figure 3.4 and Figure 3.5. Once the optimal linear weights are determined, the combination of sub-stencils provides 5<sup>th</sup> order accuracy in smooth field. Authors of [31]

mentioned the linear weight can be calculated by Lagrange interpolation basis, but no more details are provided. In this section, we introduce the method of constructing WENO 2D with 3<sup>rd</sup> and 5<sup>th</sup> order by least square method.

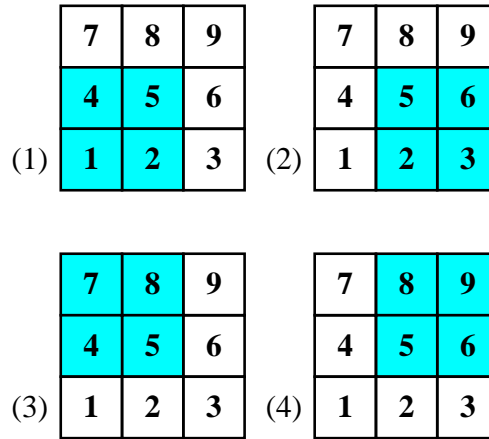


Figure 3.4 Stencils of 3<sup>rd</sup> order WENO 2D. The high order stencil contains cells 1~9, blue ones represent the cells in sub-stencils (1) ~ (4).

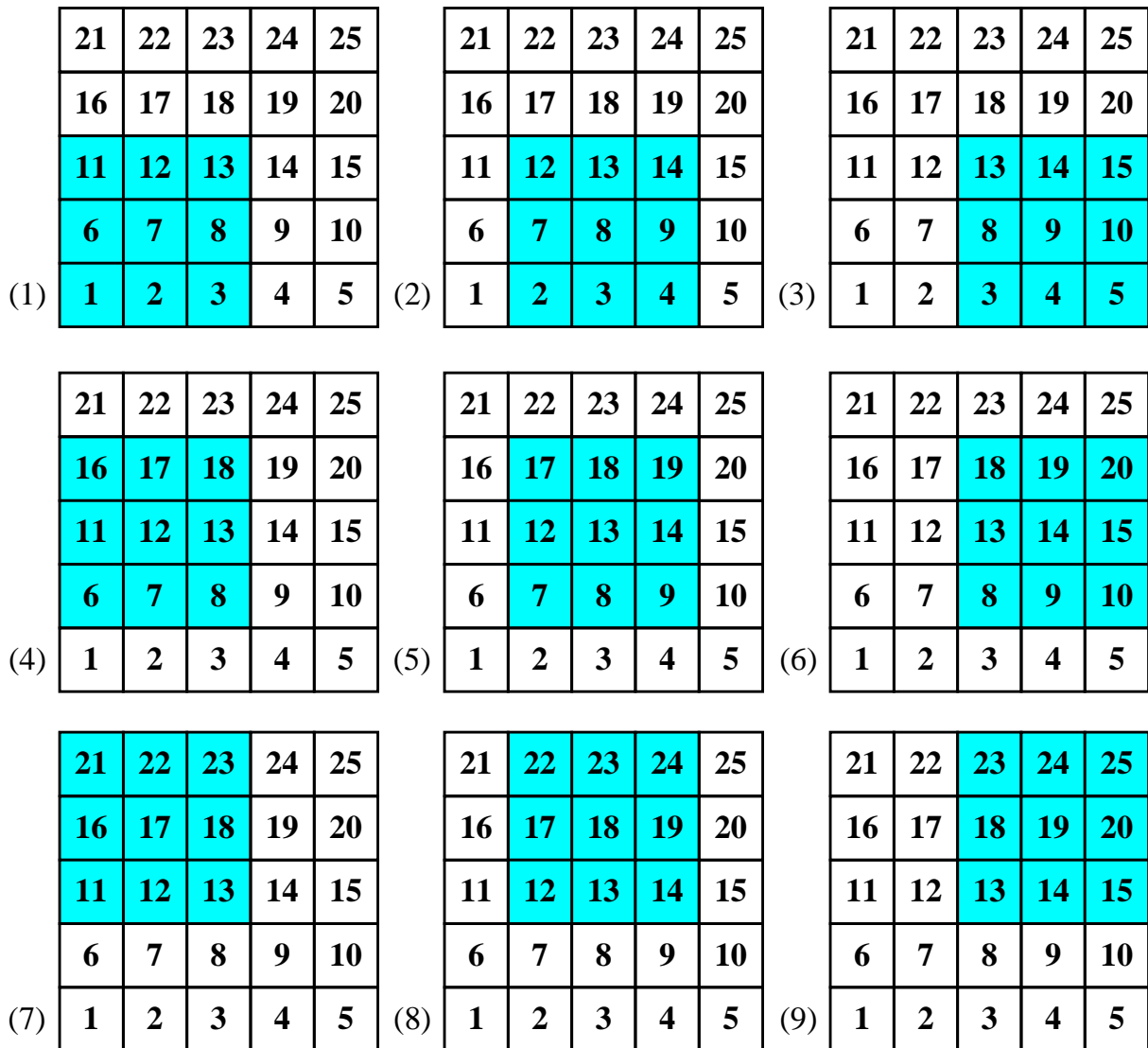


Figure 3.5 Stencils of 5<sup>th</sup> order WENO 2D. The high order stencil contains cells 1~25, blue ones represent the cells in sub-stencils (1) ~ (9).

We construct WENO 2D based on TPP and square stencil. As mentioned in previous section, a  $n$ -th order stencil contains

$m = n^2$  cells, and the stencil width is  $h = n$ . Decomposing the high-order stencil into  $s = \left(\frac{n+1}{2}\right)^2$  sub-stencils, there are  $s_c = s$  cells in each sub-stencil, and the sub-stencil width is  $l = \frac{n+1}{2}$ . For the reconstruction point  $(x, y)$ , suppose  $p_H(x, y)$  is the reconstruction value of high-order stencil, the reconstruction values of sub-stencils are stored in vector  $\mathbf{p} = (p_1(x, y), p_2(x, y), \dots, p_s(x, y))^T$ . The intention of constructing the optimal linear weights is to determine the unique weights  $\gamma = (\gamma_1, \gamma_2, \dots, \gamma_s)$ , such that

$$p_H = \gamma \mathbf{p} \quad (3.16)$$

For calculating  $\gamma$ , we need to write the high order and low order reconstruction matrix into the same linear system. For sub-stencil  $i$  we have reconstruction matrix  $R_i = (r_{ik}), k = 1, 2, \dots, s_c$ , which is computed by (3.15). We define  $R_{L_i} = (r_{L_{ij}}), j = 1, 2, \dots, m$  is the extension matrix of  $R_i$ , and

$$(R_i)_{1 \times s_c} (E)_{s_c \times m} = (R_{L_i})_{1 \times m}$$

subscript outside bracket represents the shape of each matrix in bracket, and the matrix  $E = (e_{ij}), i = 1, 2, \dots, s_c; j = 1, 2, \dots, m$  describes the correspondence between cells in high-order stencil and low-order stencil, when the  $i$ -th cell in low-order stencil is the same as the  $j$ -th cell in high order stencil,  $e_{ij} = 1$ , otherwise,  $e_{ij} = 0$ . The example case of the 3<sup>rd</sup> order scheme is shown in section 7, the high order situations are similar to the 3<sup>rd</sup> order case.

Expand (3.16) by (3.14) in single point case ( $M = 1$ ), yield

$$R_H \bar{\mathbf{q}} = \sum_{i=1}^s R_{L_i} \gamma_i \bar{\mathbf{q}} \quad (3.17)$$

where the elements of vector  $\bar{\mathbf{q}} = (q_1, q_2, \dots, q_m)^T$  represent VIA of each cell in high-order stencil.  $R_H = (r_{Hj}), j = 1, 2, \dots, m$  is the reconstruction matrix of high-order stencil.

We set  $R_L = (R_{L_1}, R_{L_2}, \dots, R_{L_s})^T$ , (3.17) becomes

$$R_L \gamma = R_H \quad (3.18)$$

the unknown optimal weight matrix  $\gamma$  can be determined by following least square procedure

$$\gamma = (R_L^T R_L)^{-1} R_L^T R_H \quad (3.19)$$

However, the elements of  $\gamma$  could be negative, which would cause unstable. A split technique mentioned by Shi et al. (2002)[31] was adopted to solve this problem. The optimal weights can be split into two parts:

$$\gamma^+ = \frac{\theta|\gamma| + \gamma}{2}, \quad \gamma^- = \frac{\theta|\gamma| - \gamma}{2} \quad (3.20)$$

where the constant  $\theta = 3$ . The reconstruction value on point  $(x, y)$ :

$$q(x, y) = \sum_{i=1}^s (\omega_i^+ - \omega_i^-) p_i(x, y) \quad (3.21)$$

We want the nonlinear weight  $\omega_i$  is large when stencil  $i$  is smooth on target cell and if stencil  $i$  is discontinuous,  $\omega_i$  should be a small value. There are serial choices of nonlinear weight scheme WENO-JS[11], WENO-Z[3], WENO-Z+[1],

WENO-Z+M[21] and so on. In this paper, we adopt WENO-Z scheme, most of WENO schemes are developed based on one-dimensional case, we extend WENO-Z to a two-dimensional case by modifying  $\tau$ , which is an important coefficient for high order WENO-Z. For stencil  $i$  the nonlinear weight is given as

$$\omega_i^\pm = \frac{\alpha_i^\pm}{\sum_{i=1}^s \alpha_i^\pm} \quad (3.22)$$

$$\alpha_i^\pm = \gamma_i^\pm \left( 1 + \frac{\tau}{\beta_i + \varepsilon} \right) \quad (3.23)$$

$$\tau = \frac{2}{(s+1)s} \sum_{\eta=1}^{s-1} \sum_{\psi=\eta}^s |\beta_\psi - \beta_\eta| \quad (3.24)$$

The smooth indicators  $\beta_i$  measure how smooth the reconstruction functions are in the target cell, we use a similar scheme as described in [44]:

$$\beta_j = \sum_{\zeta=1}^m \iint_{\Omega} \frac{\partial^\zeta}{\partial x^{\zeta_1} \partial y^{\zeta_2}} p_j(x, y) dx dy \quad (3.25)$$

where  $\zeta_1 + \zeta_2 = \zeta$  and  $\zeta > 0$ ,  $\zeta_1, \zeta_2 \in [0, n]$ .

### 3.3 Treatment of the Panel Boundaries

The cubed sphere grid comprises eight panel boundaries, and the flux across the interface between any two panels must be computed at the quadrature points situated on the edges of the boundary cells, as depicted in Figure 3.6 (a). However, a challenge arises because the coordinates across these panel boundaries are discontinuous. Given that the TPP reconstruction necessitates a square stencil, the values of the cells outside the domain (referred to as ghost cells) must be computed through interpolation within the adjacent panel, as illustrated in Figure 3.6 (b). Ullrich et al. (2010) [34] proposed a one-side interpolation scheme, but in our test, we found that using one-sided interpolation around panel boundaries leads to instability when the accuracy exceeds the 7th order.

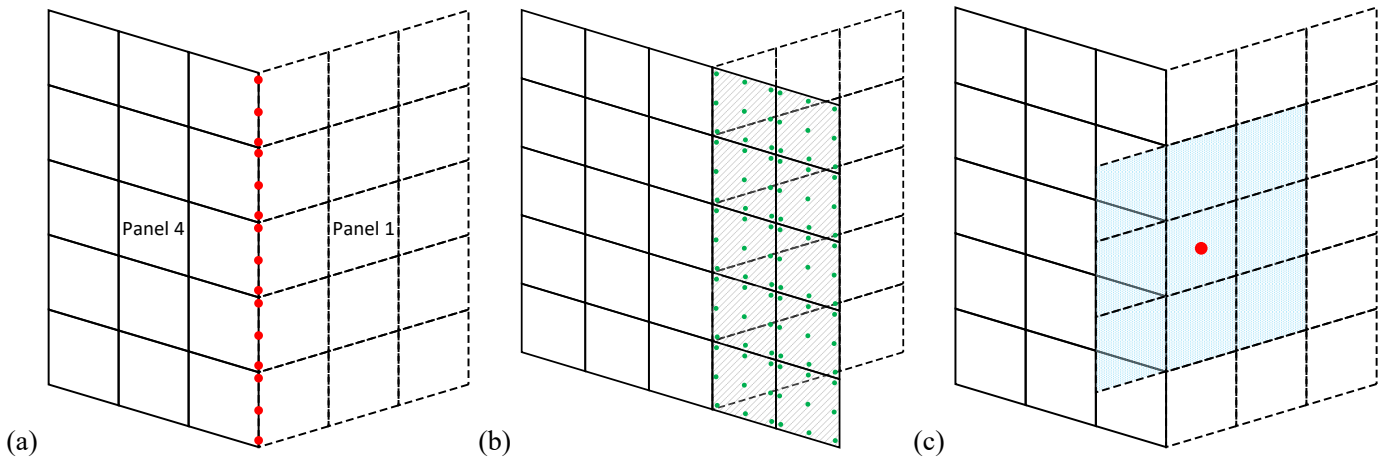


Figure 3.6 Points and cells close to panel boundary. (a) Flux points on the interface between Panel 1 and Panel 4, the flux across each panel at these points are determined by Riemann solver, which merges the reconstruction outcomes from both panels into a single flux value; (b) Ghost cells (shaded cells) out of Panel 4 boundary, with green points representing the GQP in these cells; (c) Cells requirement for 3<sup>rd</sup> order ghost cell interpolation stencil, red point represents arbitrary GQP which is in the ghost cell on

Panel 4, the blue shaded region represents the TPP reconstruction stencil (on Panel 1) to interpolate this red GQP.

### 3.3.1 Ghost Cell Interpolation

To achieve arbitrary high order accuracy, we attempt to devise a ghost cell interpolation scheme that incorporates information from both sides of the panel boundary. It's clear that the ghost cell values are unknown prior to interpolation, our preliminary idea is estimating the ghost cell values through an iterative process. Specifically, the method entails repeatedly performing the ghost cell interpolation until the increments of the cell values converge to zero.

Through mathematical analysis, we found that this iterative process is able to be express as a linear mapping, the iteration is no longer necessary, the detailed derivation is provided in the appendix. However, obtaining the mapping matrix of the interpolation process, we have to compute a large inverse matrix, which is not only computationally expensive, but also incurs too large memory requirements. To overcome this challenge, we implement the iterative interpolation process in PyTorch code, and leverage its automatic differentiation capability to directly obtain the interpolation matrix.

With reference to the appendix, we introduce the process of this method. Firstly, we initialize all of the ghost cell values to zero, denoted as  $\mathbf{g}^{(0)} = 0$ , the superscript indicates the iteration number. Secondly, interpolating the GQP in the ghost cells by TPP stencil. To illustrate, consider two adjacent panels shown in Figure 3.6(a). For any out-domain cell in panel 4 (shaded cell in Figure 3.6(b)), the GQPs in the cell are actually locating in panel 1. We interpolate the GQPs using the TPP stencil depicted in Figure 3.6(c), which includes some ghost cells of panel 1. After interpolating all of the GQPs, the ghost cell values using the Gaussian quadrature Eq.(3.6), obtaining  $\mathbf{g}^{(1)}$ . We then compute the norm 2 residual  $r^{(k)} = \|\mathbf{g}^{(k+1)} - \mathbf{g}^{(k)}\|_2$ . Repeat the second step until  $r^{(k)} < \epsilon$ , with  $\epsilon = 1 \cdot e^{-14}$  for double precision and  $\epsilon = 1 \cdot e^{-5}$  for single precision. In practical applications, we have observed that the iteration typically converges within fewer than 10 loops, hence we set the loop count to 10 for consistency. After this stage, we have obtained the mapping from known cells to ghost cells  $G: \mathbf{q} \rightarrow \mathbf{g}$ . According to Eq.(7.12) in appendix, this mapping is linear, implying  $G = \frac{\partial \mathbf{g}}{\partial \mathbf{q}}$  is a linear matrix, we can easily compute this derivative by using “autograd” function in PyTorch.

### 3.3.2 Fields Conversion Between Panels

The coordinates on panels are different. To explain the method of conversion fields between panels, we provide an example between panel 1 and 4. As shown in Figure 3.6(a), the flux points are shared by two panels, the coordinates are discontinuous on the panel interface. Consequently, we must reset the metric on mass variable, and the coordinate of wind vectors are also need to be converted from one panel to the other.

Suppose  $\mathbf{q}_1 = [(\sqrt{G}\phi)_1, (\sqrt{G}\phi u)_1, (\sqrt{G}\phi v)_1]^T$  and  $\mathbf{q}_4 = [(\sqrt{G}\phi)_4, (\sqrt{G}\phi u)_4, (\sqrt{G}\phi v)_4]^T$  represent the fields on panel 1 and 4. The mass field conversion from panel 4 to panel 1 is expressed by

$$(\sqrt{G}\phi)_4^1 = \frac{\sqrt{G_4}}{\sqrt{G_1}}(\sqrt{G}\phi)_1 \quad (3.26)$$

the subscript represents the target panel and the superscript stands for source panel.

The momentum vector is converted by two steps. Firstly, we convert the contravariant momentum from panel 1 to spherical momentum by matrix  $J$  as we mentioned in Eq.(2.10), then convert spherical momentum to contravariant momentum in panel 4.

$$\begin{pmatrix} (\sqrt{G}\phi u_s)_1 \\ (\sqrt{G}\phi v_s)_1 \end{pmatrix} = J_1 \begin{pmatrix} (\sqrt{G}\phi u)_1 \\ (\sqrt{G}\phi v)_1 \end{pmatrix} \quad (3.27)$$

$$\begin{pmatrix} (\sqrt{G}\phi u)_4 \\ (\sqrt{G}\phi v)_4 \end{pmatrix} = J_4^{-1} \frac{\sqrt{G_4}}{\sqrt{G_1}} \begin{pmatrix} (\sqrt{G}\phi u_s)_1 \\ (\sqrt{G}\phi v_s)_1 \end{pmatrix} \quad (3.28)$$

where  $J_1$  is the  $J$  matrix on panel 1,  $J_4^{-1}$  is the inverse matrix of  $J$  on panel 4. Obviously, the vector conversion is linear, therefore Eq.(3.27) and Eq.(3.28) can be merged into following equation

$$\begin{pmatrix} (\sqrt{G}\phi u)_4 \\ (\sqrt{G}\phi v)_4 \end{pmatrix} = C \begin{pmatrix} (\sqrt{G}\phi u)_1 \\ (\sqrt{G}\phi v)_1 \end{pmatrix} \quad (3.29)$$

where matrix  $C = \frac{\sqrt{G_4}}{\sqrt{G_1}} J_4^{-1} J_1$ .

The mass and vector are also need to be converted on GQPs in the same manner.

### 3.4 Riemann Solver

After performing spatial reconstruction, two distinct reconstruction outcomes emerge on either side of a given point location, as noted by Chen et al. (2013) [4], since the majority of atmospheric flow speeds correspond to small Mach numbers, we adopt the Low Mach number Approximate Riemann Solver (LMARS) as Riemann solver to determine the flux at the edge quadrature points.

Spatial reconstruction gives the left and right state vector,

$$\mathbf{q}_L = \begin{bmatrix} (\sqrt{G}\phi)_L \\ (\sqrt{G}\phi u)_L \\ (\sqrt{G}\phi v)_L \end{bmatrix}, \quad \mathbf{q}_R = \begin{bmatrix} (\sqrt{G}\phi)_R \\ (\sqrt{G}\phi u)_R \\ (\sqrt{G}\phi v)_R \end{bmatrix} \quad (3.30)$$

First of all, we convert the contravariant wind  $u$  to physical speed  $u^\perp$  that is perpendicular to the cell edge.

$$u^\perp = \frac{u}{\sqrt{G^{ii}}}, \quad i = \begin{cases} 1, & x \text{ direction} \\ 2, & y \text{ direction} \end{cases} \quad (3.31)$$

The wind speed  $m^*$  and geopotential height  $\phi$  are calculated by

$$m^* = \frac{1}{2} \left( u_L^\perp + u_R^\perp - \frac{\phi_R - \phi_L}{c} \right) \quad (3.32)$$

$$\phi = \frac{1}{2} [\phi_L + \phi_R - c(u_R^\perp - u_L^\perp)] \quad (3.33)$$

$$c = \frac{c_L + c_R}{2} \quad (3.34)$$

$$c_L = \sqrt{\phi_L}, c_R = \sqrt{\phi_R} \quad (3.35)$$

$c$  is the phase speed of external gravity wave, the subscript  $L, R$  represent the left and right side of cell edge.

Once  $m^*$  is determined, we need to convert it back to contravariant speed by

$$m = m^* \sqrt{G^{ii}} \quad (3.36)$$

The flux across the cell edge is then given by

$$\mathbf{F} = \frac{1}{2} [m(\mathbf{q}_L + \mathbf{q}_R) - \text{sign}(m)(\mathbf{q}_R - \mathbf{q}_L)] + \mathbf{P} \quad (3.37)$$

$$\mathbf{P} = \begin{pmatrix} 0 \\ \frac{1}{2} \sqrt{G} G^{1i} \phi_t^2 \\ \frac{1}{2} \sqrt{G} G^{2i} \phi_t^2 \end{pmatrix}, \quad i = \begin{cases} 1, & x \text{ direction} \\ 2, & y \text{ direction} \end{cases} \quad (3.38)$$

For calculation of  $\mathbf{H}$  the method is similar.

### 3.5 Temporal Integration

We use the explicit Runge-Kutta (RK) as time marching scheme, Wicker and Skamarock (2002) described a 3<sup>rd</sup> order RK with three stages[37], for the prognostic fields  $\mathbf{q}$ , the integration step from time slot  $n$  to  $n + 1$ :

$$\mathbf{q}^* = \mathbf{q}^n + \frac{\Delta t}{3} \left( \frac{\partial \mathbf{q}^n}{\partial t} \right) \quad (3.39)$$

$$\mathbf{q}^{**} = \mathbf{q}^* + \frac{\Delta t}{2} \left( \frac{\partial \mathbf{q}^*}{\partial t} \right) \quad (3.40)$$

$$\mathbf{q}^{n+1} = \mathbf{q}^n + \Delta t \left( \frac{\partial \mathbf{q}^{**}}{\partial t} \right) \quad (3.41)$$

where  $\Delta t$  is the time step, and temporal tendency terms  $\frac{\partial \mathbf{q}}{\partial t}$  can be obtain by (2.15), (2.16).

## 4. High Performance Implementation and Automatic Differentiation

The spatial operator and temporal integration of HOPE can be easily implemented using PyTorch. Specifically, the spatial reconstruction given by Eq.(3.14) is analogous to a convolution operation, while the Gaussian quadrature can be efficiently expressed as a matrix-vector multiplication. Both of these operations are highly optimized for execution on GPUs, ensuring superior performance. Furthermore, as a versatile platform for AI development, PyTorch offers automatic differentiation capabilities for all the aforementioned functions, streamlining the implementation and enabling efficient gradient computation. All of our tests are based on a platform of Ubuntu 22.04 LTS system with the hardware of dual intel E5-2699V4 512GB DDR4 2400 MHz and a NVIDIA RTX 3090 24GB GDDR6X.

For the reconstruction implementation. Suppose the cubed sphere grid comprises  $n_c$  cells in  $x$ -direction within each panel, including ghost cells. The panel number is  $n_p$ , and the shallow water equation involves  $n_v$  prognostic variables, we write the cell state tensor  $\mathbf{q}$  with the shape  $(n_v n_p, 1, n_c, n_c)$ . The TPP reconstruction weight tensor  $\mathbf{R}$  has shape  $(n_{poc}, 1, s_w, s_w)$ , where  $n_{poc}$  is the number of points required to be interpolated within each cell (including EQP and CQP),



$s_w$  denotes the stencil width. The reconstruction can be executed by a simple command (pseudo-code):

$$\mathbf{q}_{rec} = torch.nn.functional.conv2d(\mathbf{q}, \mathbf{R}) \quad (4.1)$$

where the shape of  $\mathbf{q}_{rec}$  is  $(n_v, n_p, n_{poc}, n_c, n_c)$

For the Gaussian quadrature implementation. Suppose the edge state tensor  $\mathbf{q}_e$  with the shape  $(n_v, n_p, n_c, n_c, n_{poe})$ , where  $n_{poe}$  is the number of quadrature points on each edge. The edge Gaussian quadrature weight tensor  $\mathbf{g}_e$  has shape  $(n_{poe})$ . The quadrature is expressed by:

$$\mathbf{q}_g = torch.matmul(\mathbf{q}_e, \mathbf{g}_e) \quad (4.2)$$

where the shape of  $\mathbf{q}_g$  is  $(n_v, n_p, n_c, n_c)$

After spatial reconstruction, the resulting data is utilized in the Riemann solver for EQPs and for source term computation on CQPs. Subsequently, integration is performed on both EQPs and CQPs to calculate the net flux and the cell-averaged source term tendency. However, there is a dimensionality mismatch between the reconstructed points, i.e.  $n_{poc}$  is the first dimension of  $\mathbf{q}_{rec}$ , while  $n_{poe}$  is the last dimension of  $\mathbf{q}_e$ . To address this dimensionality issue, two methods are available. The first method involves rearranging the  $n_{poc}$  dimension to the last position using the “torch.tensor.permute” operation in PyTorch, This allows Gaussian integrations to be naturally implemented through the "torch.matmul" operation. The second method, which avoids the need for the "permute" operation, maintains the original dimension sequence. Instead, Gaussian integrations are performed using the "torch.einsum" function. This function sums the product of the elements of the input arrays along dimensions specified using a notation based on the Einstein summation convention.

$$\mathbf{q}_g = torch.einsum('vmpij, p \rightarrow vnij', \mathbf{q}_e, \mathbf{g}_e) \quad (4.3)$$

We have conducted performance tests comparing the two methods, and the results indicate that the second method is approximately 5% faster than the first. Specifically, the first method took 649 seconds, while the second method took 616 seconds. The test was set as a one-day steady state geostrophic flow (with details provided in section 5.1) simulation at a resolution of  $0.1^\circ$ , using 3<sup>rd</sup> order accuracy reconstruction stencil. The time step was 30 seconds, and the default data type used was “torch.float32” (single precision).

The Riemann solver implementation on flux points is way easier, only needs to call “torch.sign” for Eq.(3.37), while all other operations can be executed using basic arithmetic: addition, subtraction, multiplication, and division. During a Runge-Kutta sub-step, there are no dependencies, and neither "for" loops nor "if" statements are required in the HOPE kernel code. This algorithm fully leverages the capabilities of the GPU.

## 5. Numerical Experiments

The standard test cases for spherical shallow water model are mentioned by Williamson et al. (1992)[38]. In this article, we test HOPE dynamic core using case number 2, 5, 6 desired in [38], and the case of perturbed jet flow mentioned in [7]. Besides, to prove the ability of the HOPE model in capturing shock waves, we have designed a dam-break experiment.

## **5.1 Global Steady State Nonlinear Zonal Geostrophic Flow**

## **5.2 Zonal Flow over an Isolated Mountain**

## **5.3 Rossby-Haurwitz Wave with 4 Waves**

## **5.4 Perturbed Jet Flow**

## **5.5 Dam-Break Experiment for Shock Wave Capturing**

## **6. Conclusions**

In this article, we introduce HOPE, an innovative high-order finite volume model capable of achieving arbitrary odd-order convergence. During the 11<sup>th</sup>-order accuracy test with  $2^\circ \times 2^\circ$  coarse grid, the simulation error approached the level of machine precision error. Furthermore, HOPE has also exhibited excellent performance in other numerical test cases. The algorithm of HOPE can effectively leverage the performance of GPUs. Spatial reconstructions are implemented using convolution operators, and integration operations are equivalent to matrix-vector multiplications, both of which are widely utilized in the field of machine learning. Additionally, HOPE has been developed using PyTorch, thereby inherently benefiting from its automatic differentiation capability. This makes it straightforward to integrate HOPE with any neural network (NN) system, allowing for the construction of a hybrid prediction model that combines a high-order, high-performance numerical dynamic core with an NN-based physical parameterization package. In our ongoing research, we are constructing a two-dimensional non-hydrostatic fully compressible model utilizing a finite volume method similar to that employed in HOPE.

## 7. Appendix

In this appendix, we introduce a novel boundary ghost cell interpolation scheme for cubed sphere, which is able to support HOPE to reach the accuracy over 11<sup>th</sup> order or even higher.

There are two types of cells, in-domain and out-domain (also named ghost cell, as show in Figure 3.6(b)), we define the set of in-domain cell values  $\mathbf{q}_{d \times 1} = (q_1, q_2, \dots, q_d)^T$ , the set of out-domain cell values  $\mathbf{g}_{h \times 1} = (g_1, g_2, \dots, g_d)^T$ , and the set of Gaussian quadrature point values (green points in Figure 3.2) in out-domain cells is define as  $\mathbf{v}_{p \times 1} = (v_1, v_2, \dots, v_p)$ . To identify the shape of the arrays, we denote the array shape using subscripts (this convention will be followed throughout the subsequent text). The purpose of ghost cell interpolation is using the known cell value  $\mathbf{q}$  to interpolate the unknown  $\mathbf{g}$ .

Define a new set includes the values of domain cell values and ghost cell values

$$\tilde{\mathbf{q}}_{(d+h) \times 1} = \mathbf{q} \cup \mathbf{g} = (q_1, q_2, \dots, q_d, g_1, g_2, \dots, g_h)^T \quad (7.1)$$

Similar to the describe in section 3.1, we can use a TPP to reconstruct the ghost quadrature points

$$\mathbf{v}_{p \times 1} = A_{p \times (d+h)} \tilde{\mathbf{q}}_{(d+h) \times 1} \quad (7.2)$$

where  $A_{p \times (d+h)}$  is the interpolation matrix that can be obtain by the similar method to (3.11). The ghost cell values are calculated by Gaussian quadrature

$$\mathbf{g}_{h \times 1} = B_{h \times p} \mathbf{v}_{p \times 1} \quad (7.3)$$

where  $B_{h \times p}$  is the Gaussian quadrature matrix.

$\tilde{\mathbf{q}}_{(d+h) \times 1}$  can be decomposed as the linear combination of  $\mathbf{q}_{d \times 1}$  and  $\mathbf{v}_{p \times 1}$

$$\tilde{\mathbf{q}}_{(d+h) \times 1} = \begin{pmatrix} I_{d \times d} & 0 \\ 0 & B_{h \times p} \end{pmatrix} \begin{pmatrix} \mathbf{q}_{d \times 1} \\ \mathbf{v}_{p \times 1} \end{pmatrix} = \tilde{B}_{(d+h) \times (d+p)} \bar{\mathbf{q}}_{(d+p) \times 1} \quad (7.4)$$

where  $I_{d \times d}$  is an identity matrix, and

$$\tilde{B}_{(d+h) \times (d+p)} = \begin{pmatrix} I_{d \times d} & 0 \\ 0 & B_{h \times p} \end{pmatrix} \quad (7.5)$$

$$\bar{\mathbf{q}}_{(d+p) \times 1} = \begin{pmatrix} \mathbf{q}_{d \times 1} \\ \mathbf{v}_{p \times 1} \end{pmatrix} \quad (7.6)$$

Substitute Eq.(3.12) into Eq.(3.8), we have

$$\mathbf{v}_{p \times 1} = A_{p \times (d+h)} \tilde{B}_{(d+h) \times (d+p)} \bar{\mathbf{q}}_{(d+p) \times 1} = \tilde{A}_{p \times (d+p)} \bar{\mathbf{q}}_{(d+p) \times 1} = \tilde{A}_{p \times (d+p)} \begin{pmatrix} \mathbf{q}_{d \times 1} \\ \mathbf{v}_{p \times 1} \end{pmatrix} \quad (7.7)$$

We found that matrix  $\tilde{A}_{p \times (d+p)}$  can be decomposed into two parts

$$\tilde{A}_{p \times (d+p)} = (\bar{A}_{p \times d} \quad C_{p \times p}) \quad (7.8)$$

Such that

$$\mathbf{v}_{p \times 1} = \bar{A}_{p \times d} \mathbf{q}_{d \times 1} + C_{p \times p} \mathbf{v}_{p \times 1} \quad (7.9)$$

Therefore

$$(I_{p \times p} - C_{p \times p}) \mathbf{v}_{p \times 1} = \bar{A}_{p \times d} \mathbf{q}_{d \times 1} \quad (7.10)$$

We set  $D_{p \times p} = I_{p \times p} - C_{p \times p}$ , then  $\mathbf{v}_{p \times 1}$  can be determined by

$$\mathbf{v}_{p \times 1} = D_{p \times p}^{-1} \bar{A}_{p \times d} \mathbf{q}_{d \times 1} \quad (7.11)$$

Substitute Eq.(7.11) into Eq.(7.3), we establish the relationship between ghost cell values and in-domain cell values

$$\mathbf{g}_{h \times 1} = B_{h \times p} \mathbf{v}_{p \times 1} = B_{h \times p} D_{p \times p}^{-1} \bar{A}_{p \times d} \mathbf{q}_{d \times 1} = G_{h \times d} \mathbf{q}_{d \times 1} \quad (7.12)$$

where  $G_{h \times d} = B_{h \times p} D_{p \times p}^{-1} \bar{A}_{p \times d}$ . It's clear that Eq.(7.12) is linear, and only rely on the mesh and Gaussian quadrature scheme. Therefore, we need to compute the projection matrix  $G_{h \times d}$  only once for a given mesh and accuracy, this matrix can be computed by a preprocessing system and save it to the hard disk.

## 8. References

- [1] Acker F., Borges B. de R. Borges, Costa, B. An improved WENO-Z scheme. *Journal of Computational Physics*, 313, 726-753, 2016.
- [2] Bi, K., Xie, L., Zhang, H., Chen, X., Gu, X., Tian, Q. Accurate medium-range global weather forecasting with 3D neural networks. *Nature*, 619, 533-538, 2023.
- [3] Borges R., Carmona, M., Costa, B., Don, W. An improved weighted essentially non-oscillatory scheme for hyperbolic conservation laws. *Journal of Computational Physics*, 227, 3191-3211, 2008.
- [4] Chen, X., Andronova, N., Van L., Bram, P., Joyce E., Boyd, J. P., Jablonowski, C., Lin, S.-J.. A Control-Volume Model of the Compressible Euler Equations with a Vertical Lagrangian Coordinate. *Monthly Weather Review*, 141, 2526-2544, 2013.
- [5] Chen, Kang, Han, Tao, Chen, Xi, Ma, Leiming, Gong, Junchao, Zhang, Tianning, Yang, Xiaokang, Bai, Lei, Ling, Fenghua, Su, Rui, Ci, Yuanzheng, Ouyang, Wanli. FengWu: Pushing the Skillful Global Medium-range Weather Forecast beyond 10 Days Lead. arXiv:2304.02948v1 [cs.AI] 6 Apr 2023.
- [6] Chen, C., Xiao, F.. Shallow water model on cubed-sphere by multi-moment finite volume method. *Journal of Computational Physics*, 227, 5019-5044, 2008.
- [7] Galewsky, Joseph, Scott, Richard K., Polvani, Lorenzo M. An Initial-Value Problem for Testing Numerical Models of the Global Shallow-Water Equations. *Tellus*, 56A, 429-440, 2004.
- [8] Hu, C., Shu, C.-W. Weighted Essentially Non-oscillatory Schemes on Triangular Meshes. *Journal of Computational Physics*, 150, 97-127, 1999.
- [9] Huang, L., Chen, D., Deng, L., Xu, Z., Yu, F., Jiang, Y., Zhou, F.. Main Technical Improvements of GRAPES-Meso V4.0 and Verification (in Chinese). *Journal of Applied Meteorological Science*, 28, 25-37, 2017.
- [10] Ii, S. and Xiao F. A global shallow water model using high order multi-moment constrained finite volume method and icosahedral grid. *Journal of Computational Physics*, 229, 1774-1796, 2010.
- [11] Jiang, G.-S., Shu C.-W. Efficient Implementation of Weighted ENO Schemes. *Journal of Computational Physics*, 126, 202-228, 1996.
- [12] Katta, K. K., Nair, R. D. and Kumar, V.. High-order finite volume shallow water model on the cubed-sphere: 1D reconstruction scheme. *Applied Mathematics and Computation*, 266, 316-327, 2015.
- [13] Katta, K. K., Nair, R. D. and Kumar, V.. High-Order Finite-Volume Transport on the Cubed Sphere: Comparison between 1D and 2D Reconstruction Schemes. *Monthly Weather Review*, 143, 2937-2954, 2015.
- [14] Kochkov, Dmitrii, Yuval, Janni, Langmore, Ian, Norgaard, Peter, Smith, Jamie, Mooers, Griffin, Lottes, James, Rasp, Stephan, Duben, Peter, Klower, Milan, Hatfield, Sam, Battaglia, Peter, Sanchez-Gonzalez, Alvaro, Willson, Matthew, Brenner, Michael P., Hoyer, Stephan. Neural General Circulation Models for Weather and Climate. *Nature*, 632, 1060-1066.

- [15] Lam, Remi, Sanchez-Gonzalez, Alvaro, Willson, Matthew, Wirnsberger, Peter, Fortunato, Meire, Alet, Ferran, Ravuri, Suman, Ewalds, Timo, Eaton-Rosen, Zach, Hu, Weihua, Merose, Alexander, Hoyer, Stephan, Holland, George, Vinyals, Oriol, Stott, Jacklynn, Pritzel, Alexander, Mohamed, Shakir. Learning Skillful Medium-Range Global Weather Forecasting. *Science*, 382, 1416-1421, 2023.
- [16] Battaglia, Peter. GraphCast: Learning Skillful Medium-Range Global Weather Forecasting. arXiv:2212.12794v1 [cs.LG] 24 Dec 2022.
- [17] Liou, M.-S. A Sequel to AUSM: AUSM+. *Journal of Computational Physics*, 129, 364–382, 1996.
- [18] Liou, M.-S. A sequel to AUSM, Part II: AUSM+-up for all speeds. *Journal of Computational Physics*, 214, 137-170, 2006.
- [19] Liu, X.-D., Osher, S. and Chan T. Weighted Essentially Non-oscillatory Schemes. *Journal of Computational Physics*, 115, 200-212, 1994.
- [20] Lunet, T., Lac, C., Auguste, F., Visentin, F., Masson, V., Escobar, J. Combination of WENO and Explicit Runge–Kutta Methods for Wind Transport in the Meso-NH Model. *Monthly Weather Review*, 145, 3817-3838, 2017.
- [21] Luo, X. and Wu, S.-P. An improved WENO-Z+ scheme for solving hyperbolic conservation laws, *Journal of Computational Physics*, 445, 110608, 2021.
- [22] Malardel, S., Wedi, N., Deconinck, W., Diamantakis, M., Kühnlein, C., Mozdzyński, G., Hamrud, M., Smolarkiewicz, P. A new grid for the IFS, Meteorology section of ECMWF Newsletter, 146, 23–28, 2016.
- [23] Norman, M. R. A high-order WENO-limited finite-volume algorithm for atmospheric flow using the ADER-differential transform time discretization. *Quarterly Journal of the Royal Meteorological Society*, 147, 1661-1690, 2021.
- [24] Nair, R. D., Thomas, S. J., Loft, R. D. A Discontinuous Galerkin Transport Scheme on the Cubed Sphere. *Monthly Weather Review*, 133, 814-828, 2005.
- [25] Nair, R. D., Thomas, S. J., Loft, R. D. A Discontinuous Galerkin Global Shallow Water Model. *Monthly Weather Review*, 133, 876-887, 2005.
- [26] Nair, R. D., Choi, H. W., Tufo, H. M.. Computational aspects of a scalable high-order discontinuous Galerkin atmospheric dynamical core. *Computers & Fluids*, 38, 309-319, 2009.
- [27] Nair, R. D., Bao, L., Toy, M. D., Robert, K. A High-Order Multiscale Global Atmospheric Model. 8th AIAA Atmospheric and Space Environments Conference, 1-13, 2016.
- [28] Perkins, W. A., Brenowitz, N. D., Bretherton, C. S., Nugent, J. M. Emulation of Cloud Microphysics in a Climate Model. *Journal of Advances in Modeling Earth Systems*, 16(4), 2024.
- [29] Pressel, K. G., Kaul, C. M., Schneider, T., Tan, Z., Mishra, S. Large-eddy simulation in an anelastic framework with closed water and entropy balances. *Journal of Advances in Modeling Earth Systems*, 7, 1425-1456, 2015.
- [30] Sadourny, R. Conservative Finite-Difference Approximations of the Primitive Equations on Quasi-Uniform Spherical Grids. *Monthly Weather Review*, 100, 136-144, 1972.
- [31] Shi, J., Hu, C., Shu, C.-W.. A Technique of Treating Negative Weights in WENO Schemes. *Journal of Computational Physics*, 175, 108-127, 2002.
- [32] Straka, J. M., Wilhelmson, R. B., Wicker, L. J., Anderson, J. R., Droegemeier, K. K.. Numerical Solutions of A Non-Linear Density Current: A Benchmark Solution and Comparisons. *International Journal for Numerical Methods In Engineering*, 17, 1-22, 1993.
- [33] Shen, T., Tian, Y., Shen, D., Shen, X., Sun, X., Liang, X., Lu, W. Numerical Weather Prediction (in Chinese), 2nd

Edition., China Meteorological Press, Beijing, 487 pp, 2015.

- [34] Ullrich, P. A., Jablonowski, C., van Leer, B.. High-Order Finite-Volume Methods for the Shallow-Water Equations on the Sphere. *Journal of Computational Physics*, 229, 6104-6134, 2010.
- [35] Ullrich, P. A., Jablonowski, C.. MCore: A Non-hydrostatic Atmospheric Dynamical Core Utilizing High-order Finite-volume Methods. *Journal of Computational Physics*, 231, 5078-5108, 2012.
- [36] Wang, Xin, Han, Yilun, Xue, Wei, Yang, Guangwen, Zhang, Guang J. Stable Climate Simulations Using a Realistic General Circulation Model with Neural Network Parameterizations for Atmospheric Moist Physics and Radiation Processes. *Geoscientific Model Development*, 15, 3923-3940, 2022.
- [37] Wicker, L. J., Skamarock, W. C.. Time-Splitting Methods for Elastic Models Using Forward Time Schemes. *Monthly Weather Review*, 130, 2088-2097, 2002.
- [38] Williamson, D. L., Drake, J. B., Hack, J. J., Jakob, R., and Swarztrauber, P. N.: A Standard Test Set for Numerical Approximations of the Shallow Water Equations in Spherical Geometry, *J. Comput. Phys.*, 102, 211–224, 1992.
- [39] Sun, Q., Jiao, R., Xia, J., Yan, Z., Li, H., Sun, J., Wang, L., Liang, Z.. Adjusting Wind Speed Prediction of Numerical Weather Forecast Model Based on Maching Learning Methods. *Meteorological Monthly*, 45(3), 426-436. 2019 (in Chinese).
- [40] Zeng, Q.. *Mathematical and Physical Bases of Numerical Weather Prediction, Volume 1* (in Chinese), Beijing: Science Press, 1979.
- [41] Zhang, Y., Long, M., Chen, K., Xing, L., Jin, R., Jordan, M. I., Wang, J. Skilful Nowcasting of Extreme Precipitation with NowcastNet. 619, 536-532, 2023.
- [42] Zhao, F., Pan, L., Wang S.. Weighted essentially non-oscillatory scheme on unstructured quadrilateral and triangular meshes for hyperbolic conservation laws. *Journal of Computational Physics*, 374, 605-624, 2018.
- [43] Zhu, J., Shu, C.-W.. A New Type of Multi-resolution WENO Schemes with Increasingly Higher Order of Accuracy. *Journal of Computational Physics*, 375, 659–683, 2018.
- [44] Zhu, J., Shu, C.-W.. A New Type of Multi-resolution WENO Schemes with Increasingly Higher Order of Accuracy on Triangular Meshes. *Journal of Computational Physics*, 392, 19-33, 2019.
- [45] Zhu, J., Qiu, J.. New Finite Volume Weighted Essentially Nonoscillatory Schemes on Triangular Meshs. *SIAM Journal on Scientific Computing*, 40, A903-A928, 2018.